



# The orientational dynamics of deformable finite-sized bubbles in turbulence

Ashik Ullah Mohammad Masuk<sup>1</sup>, Ashwanth K.R. Salibindla<sup>1</sup> and Rui Ni<sup>1</sup>,†

<sup>1</sup>Department of Mechanical Engineering, The Johns Hopkins University, Baltimore, MD 21218, USA

(Received 13 May 2020; revised 15 October 2020; accepted 18 January 2021)

We present simultaneous three-dimensional measurements of deformable finite-sized bubbles and surrounding turbulent flows. The orientations of bubbles are linked to two key mechanisms that drive bubble deformation: the turbulent strain rate and slip velocity between the two phases. The strongest preferential alignment is between the bubbles and slip velocity, indicating the latter plays a dominant role. We also compared our experimental results with the deformation of ideal material elements with no slip velocity or surface tension. Without these, material elements show highly different orientations, further confirming the importance of the slip velocity in the bubble orientation. In addition to deformation, when bubbles begin to break, their relative orientations change significantly. Although the alignment of the severely deformed bubbles with the eigenvectors of the turbulent strain rate becomes much stronger, the bubble semi-major axis becomes aligned with (rather than perpendicular to) the slip velocity through an almost 90° turn. This puzzling orientation change occurs because the slip velocity contains the contributions from both the bubble and the background flow. As the bubble experiences strong deformation, the rapid elongation of its semi-major axis leads to a large bubble velocity, which dominates the slip velocity and forces its alignment with the bubble's semi-major axis. The slip velocity thereby switches from a driving mechanism to a driven result as bubbles approach breakup. The results highlight the complex coupling between the bubble orientation and the surrounding flow, which should be included when modelling the bubble deformation and breakup in turbulence.

Key words: bubble dynamics, multiphase flow, isotropic turbulence

#### 1. Introduction

Bubbles transported by turbulent flows in nature and industrial applications are constantly deformed by the surrounding turbulent stresses. The question of how the deformation affects the bubble's orientation and translational motion constitutes one of the fundamental

† Email address for correspondence: rui.ni@jhu.edu

and practically important two-phase flow problems. Significant effort has been devoted to simpler rigid particles, including both spherical (Balachandar & Eaton 2010) and non-spherical particles (Voth & Soldati 2017), which has helped to advance both the physical understanding of turbulent two-phase flows and different numerical and experimental techniques. Adding particle deformation to these already complicated problems introduces new challenges and opportunities.

One challenge is related to the deformation and orientation dynamics of deformable bubbles/drops, which are crucial to their experienced hydrodynamic forces. For instance, the added mass (Lamb 1924; Brennen 1982, 2005; Magnaudet & Eames 2000), lift (Mathai, Lohse & Sun 2020) and drag all depend on the relative orientation of the bubbles with their surrounding flows and on the bubble aspect ratio. The direct numerical simulation has made significant progress in addressing this problem (Elghobashi 2019); however, it is often quite expensive to resolve the complex deformation of finite-sized bubbles/droplets in turbulence. As a result, only the deformation of small, sub-Kolmogorov-scale, neutrally buoyant droplets has been studied using phenomenological models (Maffettone & Minale 1998; Biferale, Meneveau & Verzicco 2014). However, most deformable bubbles in turbulence are much larger and likely to be in the inertial range. In this paper, our focus is on finite-sized deformable bubbles with volume-equivalent sphere diameter (D) in the inertial range ( $\eta \ll D \ll L$ ), where  $\eta$  is the Kolmogorov scale and L is the integral length scale. Therefore, their deformation is driven by the gradient of dynamic pressure acting on the bubble interface, rather than by viscous stresses.

Most prior investigations on the orientation of deformable bubbles are limited to simple flow configurations, e.g. viscous shear flows (in which the orientation of bubbles was measured as a function of the capillary number), size (Rust & Manga 2002; Kameda, Katsumata & Ichihara 2008), or the viscosity ratio (Müller-Fischer *et al.* 2008). In these cases, the flows were in a quasi-steady state, and the flow inertia could be neglected. A final steady state for the bubble orientation that solely depends on the balance between the flow shear and the capillary stress hence can be reached (Huber *et al.* 2014). Furthermore, significant attention has been paid to the deformation and orientation of oil droplets in steady shear flows (Guido & Greco 2001; Megías-Alguacil, Fischer & Windhab 2006; Feigl *et al.* 2007; Armandoost, Bayareh & Nadooshan 2018).

The study of bubbles/droplets deformed by viscous flows has also been extended to turbulence, although limited solely to sub-Kolmogorov-scale neutrally buoyant droplets, because droplets at this scale remain subject to viscous deformation even in turbulence. For this problem, the background turbulence is simulated first, and the orientation and deformation of droplets can be calculated by employing the same phenomenological model used by Maffettone & Minale (1998); inputs being the local turbulent vorticity and strain rates (Biferale et al. 2014). In this work, unlike small rigid non-spherical particles, e.g. rods and fibres (Shin & Koch 2005; Parsa et al. 2012; Chevillard & Meneveau 2013; Ni et al. 2015), the semi-major axis of the deformed droplets show stronger alignment with the maximum stretching direction of turbulent strain rate than with the vorticity vector, but the degree of this alignment decreases with an increasing capillary number. A similar method was also applied to sub-Kolmogorov neutrally buoyant droplets (Spandan, Lohse & Verzicco 2016) and bubbles (Spandan, Verzicco & Lohse 2017) in turbulent Taylor-Couette flows. The semi-major axis of these droplets also preferentially aligns with the maximum stretching direction, with a stronger alignment near the wall than in bulk region where the flow is more isotropic.

Finite-sized bubbles deforming in intense turbulence are in the opposite limit, where the viscous effect becomes negligible (the capillary number is much smaller than one). Owing to the limited studies in this regime, we examine another case of a bubble rising in an otherwise quiescent medium following a non-rectilinear path, where the bubble is deformed by the pressure gradient induced by buoyancy, and the bubble-size-based Reynolds number is sufficiently large. The semi-minor axis of the bubble typically aligns with its velocity (Lunde & Perkins 1998; Ellingsen & Risso 2001; Riboux, Risso & Legendre 2010; Legendre, Zenit & Velez-Cordero 2012) within less than 2° (Mougin & Magnaudet 2001; Ern *et al.* 2012), whereas both directions oscillate about the vertical axis within 30° (Riboux *et al.* 2010; Ellingsen & Risso 2001; Ern *et al.* 2012) for a wide range of bubble sizes (Luewisutthichat, Tsutsumi & Yoshida 1997). For this regime, the orientational dynamics are therefore periodic, and the oscillation of the bubble orientation is more closely related to its wake oscillation rather than to its deformation (Tayler *et al.* 2012).

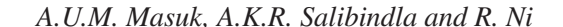
In high-Reynolds-number turbulent flows, bubbles were also observed to oscillate periodically within around 45° about the vertical axis (Ravelet, Colin & Risso 2011), which is consistent with that reported in a quiescent medium but with a slightly larger amplitude. One plausible explanation for such a similar bubble behaviour in both quiescent and turbulent media is that, in the experiment by Ravelet *et al.* (2011), turbulence was relatively weak compared with buoyancy. As a result, bubbles were still preferentially deformed by buoyancy, thereby aligning with the vertical direction. If the pressure gradient induced by turbulent stresses is stronger than that due to buoyancy, new phenomena may emerge. A recent work showed that finite-sized bubbles rising in intense turbulence experience different lift and drag forces due to the turbulence-induced deformation (Salibindla *et al.* 2020).

In the current study, we experimentally measure the bubble orientational dynamics in intense turbulence, where turbulent stresses become more important than buoyancy. The three-dimensional (3-D) shape and surrounding turbulent flows are measured simultaneously. The experimental set-up and measurement techniques used are introduced in § 2.1, whereas the measurable quantities and their calculations are summarized in § 2.2. The acquired unique data set helps us to investigate the preferential alignment of the bubble semi-major ( $\hat{r}_1$ ) and semi-minor axes ( $\hat{r}_3$ ) with the representative directions of two deformation mechanisms, i.e. the slip velocity and turbulent strain rate, which are discussed in § 3.1. Finally, the evolution of the relative orientation of the bubble with the surrounding turbulence as it approaches the moment of breakup is introduced and explained in § 3.2.

# 2. Experimental set-up and measurements

# 2.1. Experimental set-up

In this study, a vertical water tunnel named V-ONSET was utilized to measure the interaction between deforming air bubbles and surrounding turbulence. V-ONSET was designed to generate intense turbulence with a large mean energy dissipation rate  $\langle \epsilon \rangle$  of O(0.1) m<sup>2</sup> s<sup>-3</sup> while maintaining a nearly homogeneous and isotropic environment over a measurement volume of 6 cm  $\times$  6 cm  $\times$  5 cm. At this  $\langle \epsilon \rangle$ , the Kolmogorov length and time scales were determined to be  $\eta \approx 50~\mu m$  and  $\tau_{\eta} \approx 2.5$  ms, respectively. Key facility features are briefly summarized below. Additional details concerning the experimental rig and its flow characteristics can be found in Masuk *et al.* (2019*b*).



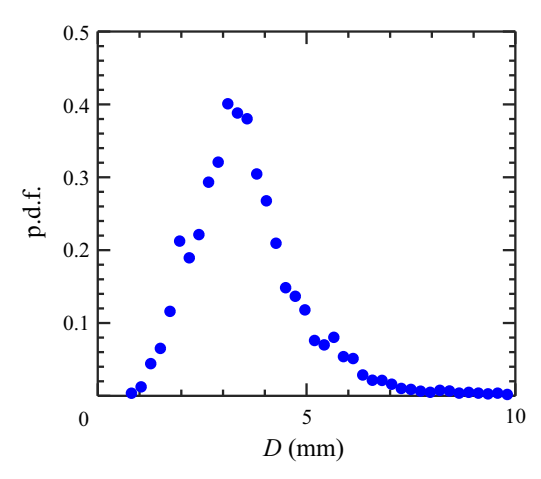


Figure 1. The distribution of the volume-equivalent sphere diameter D of all bubbles in our experiments.

In the test section of V-ONSET, intense turbulence was generated by firing high-speed momentum jets (up to 12 m s<sup>-1</sup>) into the test section through randomly selected nozzles (the nozzle diameter d is 5 mm) from a jet array. On average, 12.5% of the total 88 jets were kept activated since this was found to maximize the turbulence intensity, and their firing pattern was randomized following a Gaussian distribution. This firing scheme follows the work by Variano, Bodenschatz & Cowen (2004), to ensure that no secondary flow structure would develop in the test section (De Silva & Fernando 1994; Srdic, Fernando & Montenegro 1996; Variano et al. 2004). The jet array was located approximately 80d above the measurement location to allow jets to be fully mixed before reaching the interrogation volume. In addition, a uniform downward mean flow, with magnitude similar to the bubble rise velocity, was introduced to keep bubbles within the measurement volume for an extended time. Moreover, bubbles were generated through four groups of hypodermic needles of two sizes, which are located at the bottom of the test section. Once a bubble reached the test section, its 3-D shape was reconstructed from the virtual-camera visual-hull method (Masuk, Salibindla & Ni 2019a). The probability density function (p.d.f.) of the volume-equivalent sphere size D of the bubbles is shown in figure 1. The typical bubble size range in the test section is approximately 2–7 mm in diameter, with most around 3-4 mm.

Six high-speed cameras were distributed all around the tunnel's octagonal test section to simultaneously acquire images of both phases from different directions. Six LED panels, one for each camera, were used to provide diffused back-lighting, which results in a white background. The dark silhouettes of large dispersed bubbles and tracer particles can be identified, segmented and eventually separated based on their contrasts from the background and their size differences (the diameter of the tracer particle is 50  $\mu$ m). After image segmentation, large bubble silhouettes were input into the 3-D shape reconstruction method, whereas the tracer locations were tracked using our in-house Shake-The-Box method (Schanz, Gesemann & Schröder 2016; Tan et al. 2020) (the code is available online @JHU-Ni-Lab on GitHub). Flow information, such as velocity and acceleration, can be calculated from these 3-D trajectories. A high concentration of tracer particles could potentially contaminate the bubble interface and modulate its boundary condition; however, this effect is less important for finite-sized bubbles because their deformation is primarily driven by inertia (or, more specifically, the gradient of dynamic pressure)

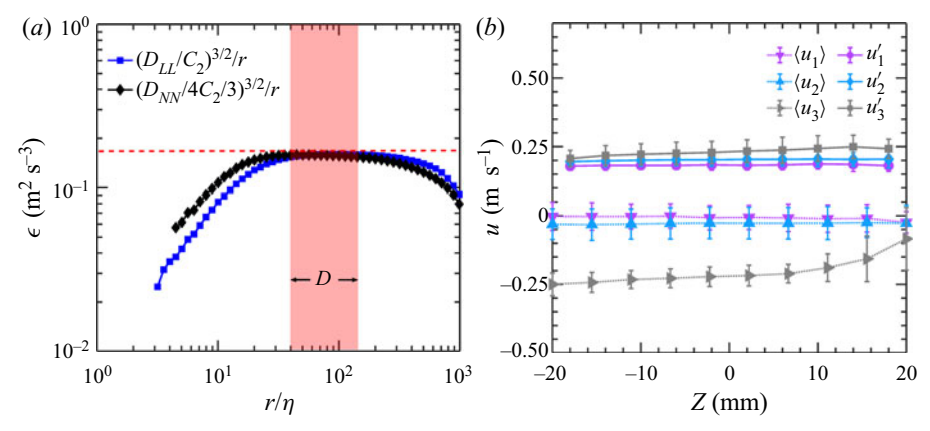


Figure 2. (a) The compensated longitudinal  $(D_{LL})$  and transverse  $(D_{NN})$  second-order structure function as a function of the separation distance between a pair of velocity vectors. (b) The profile of the mean  $\langle u_i \rangle$  and the fluctuation  $u_i'$  velocity along the vertical z axis in the view volume.

rather than by viscous stresses. Therefore, the contamination is not expected to affect the deformation statistics reported in this paper.

To confirm that the flow is indeed homogeneous and isotropic as designed, single-phase turbulence without initial bubble injection was measured by tracking tracer particles in three dimensions, whose trajectories can be used to acquire the Eulerian turbulence statistics. The results are shown here in figure 2. We first discuss the second-order Eulerian structure functions, including both the longitudinal  $(D_{LL}(r) = \langle [u_{\parallel}(\mathbf{x} + \mathbf{r}) - u_{\parallel}(\mathbf{x})]^2 \rangle)$  and transverse  $(D_{NN}(r) = \langle [u_{\perp}(\mathbf{x} + \mathbf{r}) - u_{\perp}(\mathbf{x})]^2 \rangle)$  components, where  $\langle \cdots \rangle$  represents an ensemble average over many pairs of particles with separation r. Here  $u_{\parallel}$  and  $u_{\perp}$  represent the tracer velocities projected to directions that are parallel and perpendicular to the separation direction r between a pair of particles located at x + r and x, respectively. Based on the Kolmogorov theory (Kolmogorov 1941), in the inertial range ( $\eta \ll r \ll L$ ),  $D_{LL}(r) = C_2(\langle \epsilon \rangle r)^{2/3}$  and  $D_{NN}(r) = (4/3)C_2(\langle \epsilon \rangle r)^{2/3}$ , with  $C_2$  being the Kolmogorov constant and  $D_{LL}$  and  $D_{NN}$  differing by a factor of 4/3, calculated based on the assumption that the flow is homogeneous and isotropic. To test whether the background turbulence agrees with this well-known inertial range scaling,  $D_{LL}$  and  $D_{NN}$  are compensated by the inertial range scalings and converted into the mean energy dissipation rate following  $\langle \epsilon \rangle = (D_{LL}/C_2)^{3/2}/r$  and  $\langle \epsilon \rangle = (D_{NN}/4C_2/3)^{3/2}/r$ , respectively, as shown in figure 2(a). The two compensated structure functions collapse well with each other over the inertial range where the plateau is located. Within this inertial range, the mean energy dissipation rate  $\langle \epsilon \rangle$ , measured by the plateau height (red dashed line), is found to be 0.16 m<sup>2</sup> s<sup>-3</sup>. The  $\langle \epsilon \rangle$  calculated from both structure functions are consistent with each other, suggesting that turbulence in our system is close to homogeneous and isotropic. In addition to the background turbulence, a red shaded area is added to figure 2(a) to illustrate the range of bubble sizes, which resides within the inertial sub-range as designed.

Furthermore, the spatial distributions of the mean  $\langle u_i \rangle$  (i=1,2,3) and fluctuation velocities  $u_i'$  along the vertical direction z are shown in figure 2(b). Three components of fluctuation velocities are close to each other at around 0.20 m s<sup>-1</sup>, with no obvious trend along the z-axis, further confirming that the flow is nearly homogeneous and isotropic. The mean flows along the horizontal directions  $(\langle u_1 \rangle$  and  $\langle u_2 \rangle)$  are close to zero.

To extend the bubble residence time in the view area for longer trajectories and converged statistics, the vertical mean flow  $\langle u_3 \rangle$  is designed to be at  $-0.25 \,\mathrm{m\ s^{-1}}$  to balance the rise velocity of bubbles. For bubbles rising in an otherwise quiescent water, the rise velocity of bubbles with  $D=2 \,\mathrm{mm}$  and 7 mm is about 0.25 m s<sup>-1</sup> and 0.35 m s<sup>-1</sup>, respectively (Clift, Grace & Weber 2005). As a result, the residual bubble rise velocity in the test section ranges roughly from 0 m s<sup>-1</sup> to 0.10 m s<sup>-1</sup>, which is smaller than the turbulence fluctuation velocity at around 0.20 m s<sup>-1</sup>. For more information concerning the set-up and measurement techniques, the reader can refer to Masuk *et al.* (2019*a,b*) and Tan *et al.* (2020).

# 2.2. Flow measurements and characteristics

Using the 3-D reconstructed bubble geometries, the lengths of the semi-major and semi-minor axes  $(|r_1| \text{ and } |r_3|)$  can be determined by measuring the longest and shortest distances from surface vertices to the bubble's centre-of-mass, respectively. The ratio between them is the aspect ratio, i.e.  $\alpha = |r_1|/|r_3|$ . Note that this method of extracting bubble axes does not force them to be orthogonal to each other, which captures the bubble deformation in turbulence more accurately because not all bubbles follow affine deformation in turbulence. In addition to geometrical information, the bubble trajectory can be acquired by linking the centres of the 3-D reconstructed geometries over time, which can be used to calculate the bubble velocity  $u_b$ .

From our in-house particle tracking results, the velocity  $u^p$  and acceleration  $a^p$  of the pth tracer particle at any time instant can be determined by applying a Gaussian kernel to the particle trajectory (Mordant, Crawford & Bodenschatz 2004; Ni, Huang & Xia 2012). If this tracer particle at  $x_0 + x^p$  is located near the centre of a bubble at  $x_0$  within a search radius of  $D_s/2$  ( $|x^p| < D_s/2$ ), it can be used to quantify the flow characteristics near the bubble, including the local mean flow velocity  $u_f = \sum_{p=1}^n u^p (x_0 + x^p)/n$  and velocity gradients, where n is the total number of tracer particles that can be identified within the search volume. As this study focuses on finite-sized bubbles, their alignment and orientation should be associated with flows at the bubble scale. The velocity gradients discussed hereafter are therefore referred to as  $\tilde{A}_{ij}$  with tilde representing the coarse-graining at the bubble size of D.

For  $\tilde{A}_{ij}$ , a minimum of n=4 tracer particles are needed; however, in practice, about 30–40 particles were used to perform least-squares fits by seeking the minimum value of the squared residual  $\sum_{p} [u_i^p - \tilde{A}_{ij} x_j^p]^2$  (i,j=1,2,3) (Pumir, Bodenschatz & Xu 2013; Ni *et al.* 2015; Masuk, Salibindla & Ni 2021). If these particles are located within a quasi-two-dimensional plane, estimating the out-of-plane velocity gradient would entail significant uncertainty. Therefore, similar to previous studies (Xu, Pumir & Bodenschatz 2011), an inertia tensor  $I = \sum_{p} x_i^p x_j^p / \text{tr}(\sum_{p} x_i^p x_j^p)$  was employed to evaluate the shape factor of the particle cloud. If particles are distributed uniformly in three dimensions, all three eigenvalues of the inertia tensor would be equal to 1/3; conversely, if particles lie in a plane, the smallest eigenvalue would be very close to zero. To ensure accurate estimation of velocity gradients, events with ratios between the smallest and the largest eigenvalues of the inertia tensor smaller than 0.15 were removed from the statistics. Compared with previous studies that focused on a scale closer to  $\eta$  (Ni *et al.* 2015), we require additional tracer particles for calculating  $\tilde{A}_{ij}$ .

The coarse-grained strain rate tensor,  $\tilde{S}_{ij}$ , and rotation tensor,  $\tilde{\Omega}_{ij}$ , can be obtained based on  $\tilde{A}_{ij}$ :  $\tilde{S}_{ij} = (\tilde{A}_{ij} + \tilde{A}_{ji})/2$ ,  $\tilde{\Omega}_{ij} = (\tilde{A}_{ij} - \tilde{A}_{ji})/2$ . The search volume used for calculating

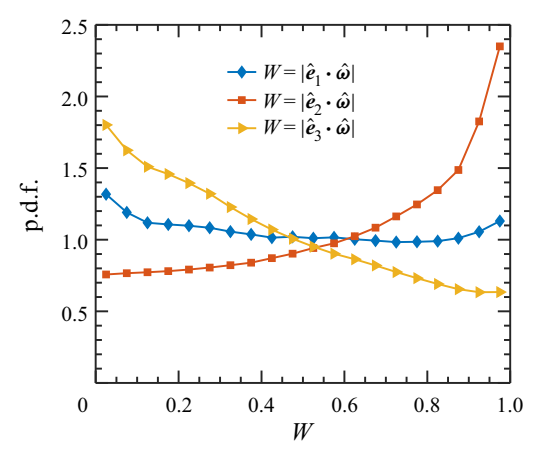


Figure 3. Probability density function of the cosine of the angle between vorticity  $\hat{\omega}$  and eigenvectors of the strain-rate tensor  $\hat{e}_i$ .

the coarse-grained velocity gradient has a different, but comparable, length scale  $D_s \approx 4D$ . The strain rate and its associated eigenvalues calculated using  $D_s$  require corrections following the method proposed by Masuk *et al.* (2021). Because both D and  $D_s$  are in the inertial range, by assuming a constant local energy dissipation rate over these scales close to the bubble size, the corrected eigenvalues of  $\tilde{S}_{ij}$  become  $\lambda_i = (\lambda_i)_s (D_s/D)^{2/3}$ , where  $(\lambda_i)_s$  represents the eigenvalues of the strain rate tensor coarse grained at the scale of  $D_s$ .

To ensure that the measured velocity gradient tensor is correct, the alignment of the coarse-grained vorticity vector  $\hat{\omega}$  with three eigenvectors of  $\tilde{S}_{ij}$ , i.e.  $\hat{e}_i$  (i=1,2,3) is shown in figure 3. Although this alignment is calculated based on the coarse-grained velocity gradient  $\tilde{A}_{ij}$ , the results are consistent with those previously reported for the local velocity gradient  $A_{ij}$  (Ashurst *et al.* 1987; Huang 1996; Xu *et al.* 2011; Ni, Ouellette & Voth 2014). In both cases, coarse-grained or not, the vorticity vector is preferentially aligned with the eigenvector corresponding to the intermediate eigenvalue of the strain rate tensor (Ni *et al.* 2014). In addition, this relative orientation is not sensitive to the range of D or  $D_s$  considered in this work, which suggests that (i) the velocity gradient measurement is successful and (ii) this preferential alignment does not depend on the selected search diameter.

# 2.3. Deformation mechanisms

A bubble can be simultaneously stretched along the maximum stretching direction  $(\hat{e}_1)$  and compressed along the maximum compression direction  $(\hat{e}_3)$  so  $\lambda$  in the dimensionless Weber number  $We_{vg} = \rho(\lambda D)^2 D/\sigma$  can be either  $\lambda_1$  or  $\lambda_3$ . Based on a recent study by Masuk *et al.* (2021), the distribution of the Weber number based on either eigenvalue seems to be nearly identical. In this paper, we intend to study the orientational dynamics of bubbles relative to  $\hat{e}_1$  and  $\hat{e}_3$  to distinguish the contribution of stretching from compression for bubble deformation.

Figure 4(a) shows an example of a bubble experiencing strong turbulent strains, illustrated by many tracer tracks that are colour-coded with their instantaneous velocity magnitude. Although the flow field is complicated and contains dynamics over multiple

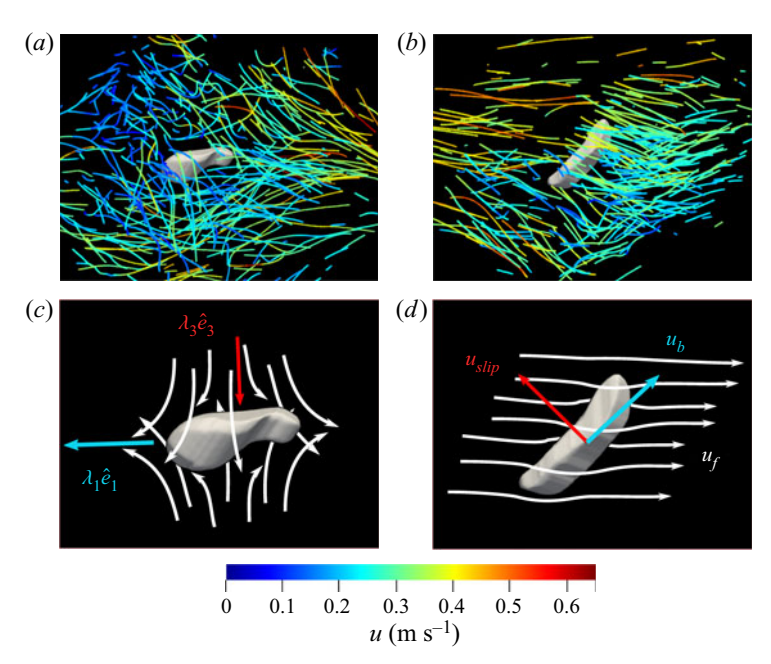


Figure 4. Reconstructed 3-D shape of deforming bubbles with surrounding tracer trajectories (the instantaneous velocity magnitude u of each particle is indicated by the colour), including (a) a case that is primarily deformed by turbulent strain and (b) another case that is primarily deformed by the slip velocity. (c,d) Schematics of the coarse-grained flow field around these two bubbles.

scales, the estimated  $\tilde{S}_{ij}$  coarse-grained at the bubble scale is sketched in figure 4(c). For this case,  $\hat{e}_3$  clearly aligns with the bubble semi-minor axis  $\hat{r}_3$ , whereas  $\hat{e}_1$  aligns with the bubble semi-major axis  $\hat{r}_1$ . This result is consistent with our expectations, but it is important to collect statistics concerning such relative orientation to ensure that this example is not an isolated case.

Another driving mechanism for bubble deformation is the slip velocity  $u_{slip} = u_b - u_f$ between the two phases. Bubbles subjected to  $u_{slip}$  will experience a motion-induced pressure gradient and thus deform, which can be measured by another Weber number:  $We_{slip} = \rho u_{slip}^2 D/\sigma$ .  $We_{slip}$  can be defined either using the total slip velocity or one of its three components, i.e.  $We_{slip,x}$ ,  $We_{slip,y}$  and  $We_{slip,z}$ . The slip velocity could arise due to multiple effects: (i) the buoyancy effect is the strongest for bubbles rising in an otherwise quiescent medium, in which the bubble deformation is primarily driven by the slip velocity along the vertical direction; (ii) the added mass force, which is important for bubbles travelling in turbulence with large carrier-phase acceleration; (iii) the finite size effect could also lead to a large slip velocity between the two phases (Bellani & Variano 2012; Cisse, Homann & Bec 2013). Figure 4(b) shows an example of a bubble subjected to a strong slip velocity along the horizontal direction. After coarse-graining the flow field, figure 4(d) illustrates the mean flow around the bubble, which is primarily along the horizontal direction. At the same time, the bubble slides along the cyan arrow. As a result, the slip velocity points in a direction indicated by the red arrow, which aligns excellently with the direction of the semi-minor axis  $\hat{r}_3$  of the reconstructed bubble geometry.

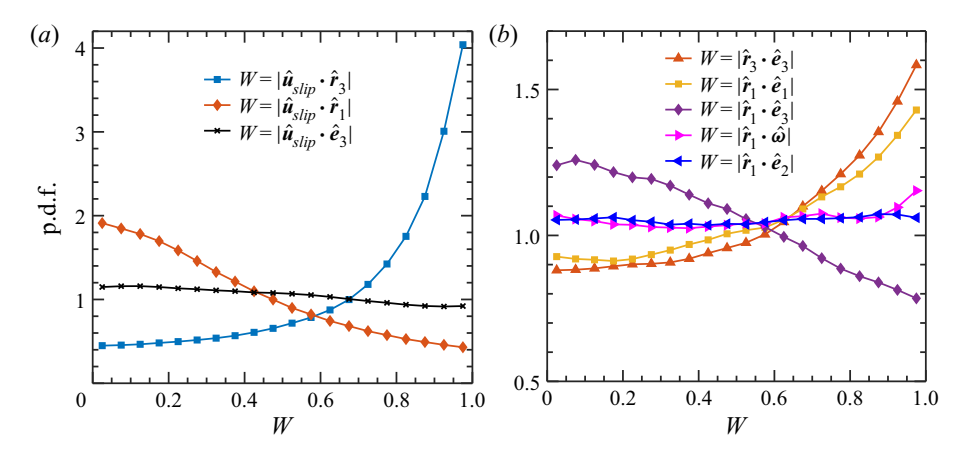


Figure 5. Probability density function of the cosine of the angle between bubble axes with (a) the slip velocity and (b) the turbulent strain rate.

#### 3. Results and discussion

# 3.1. Alignment and orientation of deforming bubbles

Figure 5 shows the p.d.f. of the cosine of the angle (W) between two unit vectors. If two unit vectors are randomly oriented, the p.d.f. should be close to a uniform distribution  $(p(W) = 1 \text{ for all } W, \text{ where } p(\cdots) \text{ represents the probability})$ . A peak at W = 1 in the p.d.f. would suggest a preferential alignment between the two vectors, whereas a peak near W = 0 would imply that the two vectors are perpendicular to each other. Figure S(a) shows the orientation of the slip velocity  $\hat{u}_{slip}$  with respect to  $\hat{r}_1$  and  $\hat{r}_3$ . There is a clear preferential alignment between  $\hat{u}_{slip}$  and  $\hat{r}_3$ , which suggests that the pressure gradient induced by the bubble's relative motion compresses the bubble along this direction.

In addition to compression, bubbles must extend in other directions to conserve volume. However,  $\hat{r}_1$  is not forced to be orthogonal to  $\hat{r}_3$  during the 3-D reconstruction to allow the capture of any non-affine deformation. Thus, the preference of  $\hat{r}_1$  being perpendicular to  $\hat{u}_{slip}$  is not as strong as that of  $\hat{r}_3$  being aligned with  $\hat{u}_{slip}$ . Such a difference also suggests that the orientation of a deformable bubble is primarily determined by the slip velocity compressing the bubble.

The contribution from the surrounding turbulent strain rate to the orientation of the bubbles is also shown in figure 5(b).  $\hat{r}_1$  and  $\hat{r}_3$  clearly preferentially align with  $\hat{e}_1$  and  $\hat{e}_3$ , respectively. The alignment between  $\hat{r}_3$  and  $\hat{e}_3$  is slightly stronger, suggesting a more important role played by the flow compression. The small difference implies that, although the bubble deformation is driven by flow compression, bubbles must be stretched along other directions with the least resistance; this happens to be  $\hat{r}_1$  if only the strain rate tensor is considered.

The preferential alignment between bubble axes with the eigenvectors of the strain rate tensor is significantly weaker compared to that with the slip velocity, despite the similarity of their respective Weber numbers (Masuk *et al.* 2021). A reason for this is that the slip velocity is associated with large-scale flow motions, which can be sustained longer compared with the strain rate. Therefore, the bubble orientation may be more dominated by the slip velocity. In addition, the slip velocity and turbulent strain rate do not always work collaboratively. Figure 5(a) shows the p.d.f. of the relative orientation between  $\hat{e}_3$  and  $\hat{u}_{slip}$ , which seems to be a nearly random distribution and may slightly prefer a perpendicular orientation. This suggests that these two mechanisms are not correlated and may even

occasionally compete with each other, and therefore a preferential alignment with the slip velocity may lead to a weaker alignment with turbulent strain rate and vice versa.

If the bubble shape can be assumed as a triaxial ellipsoid without any non-affine deformation, it can be captured as a symmetric, positive definite, second-rank tensor P. The phenomenological equation to describe the time evolution of P was provided by Maffettone & Minale (1998):

$$\frac{\mathrm{d}\boldsymbol{P}}{\mathrm{d}t} - (\boldsymbol{\Omega} \cdot \boldsymbol{P} - \boldsymbol{P} \cdot \boldsymbol{\Omega}) = -\frac{f_1}{\tau} (\boldsymbol{P} - g(\boldsymbol{P})\boldsymbol{I}) + f_2(\boldsymbol{S} \cdot \boldsymbol{P} + \boldsymbol{P} \cdot \boldsymbol{S}), \tag{3.1}$$

where S and  $\Omega$  represent the symmetric and anti-symmetric parts of the velocity gradient tensor;  $\tau = \mu D/2\sigma$  is the interfacial relaxation timescale;  $\mu$  and  $\sigma$  are the dynamic viscosity and the surface tension of water, respectively; and I is the second-rank unit tensor. The equation has two main contributions, deformation and restoration (the first term on the right-hand side), where  $f_1$  and  $f_2$  are two coefficients associated with the viscosity ratio, and g(P) is introduced to preserve the bubble volume.

Strictly speaking, equation (3.1) should not be applied to finite-sized bubbles since the model assumes a linear flow around the bubble, which should be limited solely to bubbles with size  $D \ll \eta$ . Moreover, this equation does not consider the slip velocity or the buoyancy effect owing to a significant density mismatch between the two phases. Nevertheless, when ignoring this mismatch and replacing S and  $\Omega$  with their coarse-grained counterparts, this equation can estimate the alignment between a deforming neutrally buoyant droplet and its surrounding coarse-grained strain rate.

If the restoring term led by the surface tension is ignored for further simplification, the equation restores to the deformation equation of a material element (Girimaji & Pope 1990),  $dF/dt = A \cdot F$ , where F is the deformation tensor and can be converted to a left  $C^{(L)}$  or right  $C^{(R)}$  Cauchy–Green strain tensor using  $C^{(L)} = F \cdot F^T$  and  $C^{(R)} = F^T \cdot F$ . One can prove that  $C^{(L)} \equiv P$ , which suggests that a bubble without surface tension will be deformed by turbulence similarly to the deformation process of a material element, whose three semi-major axes can be determined based on the eigenvectors of  $C^{(L)}$ . The deformation equation can be integrated to obtain  $C^{(L)}$  as reported in Ni et al. (2015), using the simulation results by Benzi et al. (2009). Although the eigenvalues of  $C^{(L)}$  grow exponentially as the integration time increases, the eigenvectors of  $C^{(L)}$ ,  $\hat{e}_{Li}$  vary by only a little and they can be used to represent the directions of neutrally buoyant droplets with zero surface tension.

Figure 6 shows the relative orientation between the semi-major axis of the deformed material element  $\hat{e}_{L1}$  with three eigenvectors,  $\hat{e}_i$ , of the strain rate tensor as well as with the vorticity vector  $\hat{\omega}$ . It has been discussed before by Ni *et al.* (2015), that the strongest alignment is observed between the semi-major axis of the material element and the vorticity vector because vorticity is amplified by the vortex stretching process. As a vortex is stretched by the Lagrangian stretching  $C^{(L)}$ , it ends up aligning with  $\hat{e}_{L1}$ .

When comparing figures 5 and 6, the semi-major axis of a material element,  $\hat{e}_{L1}$ , shows strong alignment with  $\hat{e}_2$  and  $\hat{\omega}$ , whereas the semi-major axis  $\hat{r}_1$  of finite-sized bubbles does not appear to have strong preferential orientation. This finding is qualitatively consistent with the work conducted by Biferale *et al.* (2014), who showed that, for a small capillary number, the alignment between the semi-major axis of the neutrally buoyant droplets with  $\hat{\omega}$  is relatively weak; in addition, as the capillary number increases, the alignment becomes stronger. This observation suggests that, despite the differences in Reynolds number and sizes, our results for the orientational dynamics of finite-sized

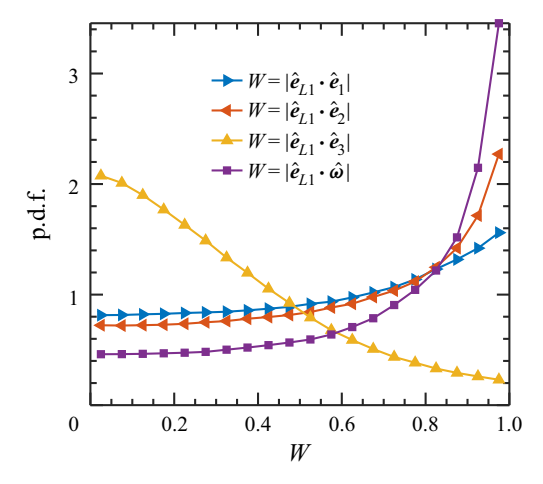


Figure 6. Probability density function of the cosine of the angle between the semi-major axis of material elements  $\hat{e}_{L1}$  and both vorticity  $\hat{\omega}$  and eigenvectors of the strain-rate tensor,  $\hat{e}_i$ .

bubbles share similarities with the sub-Kolmogorov-scale neutrally buoyant droplets at a small capillary number.

Nevertheless, the alignment of finite-sized bubbles with the coarse-grained strain rate is much weaker than that for sub-Kolmogorov-scale droplets, which is mainly caused by: (i) the competing effect from the slip velocity and (ii) the non-affine deformation allowed by our shape reconstruction method, meaning that the semi-major and semi-minor axes of the bubbles are not necessarily orthogonal, which would weaken the alignment with the eigenvectors of the coarse-grained turbulent strain rate.

# 3.2. Breakup

The previous section discussed statistics concerning the alignment between the semi-major and semi-minor axes of deforming bubbles and the slip velocity and velocity gradients. To collect sufficient statistics, bubbles with different aspect ratios and sizes were compiled together. This data can help us to answer whether the alignment depends on how strongly the bubble is deformed and whether the roles played by different mechanisms change when bubbles experience strong deformation. In this section, we will examine bubbles with strong deformation and that are close to the breakup moments, to unveil key mechanisms behind bubble breakup in turbulence.

The slip velocity and turbulent strain rate can be tracked along each bubble trajectory. For all our experiments, 190 datasets were collected, from which a total of 480 329 bubbles were reconstructed and tracked over time. The majority did not break during the time spent in the view volume, and only 195 breakup events were identified and reconstructed. Details concerning the reconstruction of the breakup events can be found in Masuk *et al.* (2019*a*) and Qi, Masuk & Ni (2020).

For all these breakup events, time traces of  $We_{slip,x}$  and  $We_{vg}$  before breakups are compiled to calculate the time evolution of the Weber numbers. Figure 7 shows the p.d.f.s of  $We_{slip,x}$  and  $We_{vg}$  at different times before breakup. The closest and the farthest times tracked before the breakup were approximately  $0.5\tau_{\eta}$  and  $20\tau_{\eta}$ , respectively. We also plot the p.d.f.s of  $We_{slip,x}$  and  $We_{vg}$  for all bubbles, including both weak and strong deformation cases, in figure 7(a,b) as black solid circles. They show that the Weber numbers for bubbles about to break are systematically larger than those for non-breaking bubbles with a

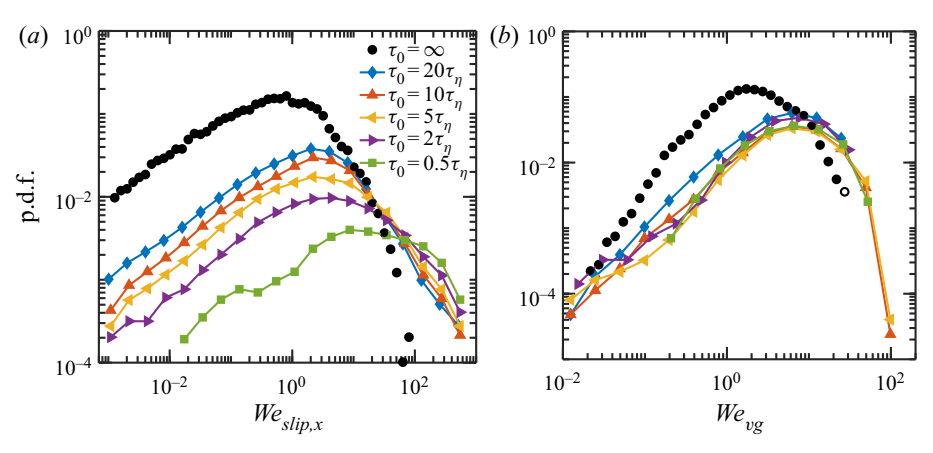


Figure 7. Probability density function of (a) the slip-velocity-based Weber number and (b) the strain-rate-based Weber number, for mild deformation case (black solid symbols) as well as different times  $(\tau_0)$  before breakup.

similar size. In addition,  $We_{slip,x}$  continues to grow from  $20\tau_{\eta}$  to  $5\tau_{\eta}$ ; however, from  $2\tau_{\eta}$  to the moment of breakup, the distribution leaps far rightward to a larger  $We_{slip,x}$ . This indicates that the bubble breakup is associated with a timescale that is within  $\sim 2\tau_{\eta}$ , over which the slip velocity experiences dramatic changes. The same calculation was performed for  $We_{vg}$ ; unlike the case for  $We_{slip,x}$ , however, the distribution of  $We_{vg}$  does not seem to experience a systematical shift over time. Nevertheless, the left tail for small  $We_{vg}$  seems to shift rightward as bubbles approach breakup, which indicates that the number of events with small velocity gradients declines near breakup. In contrast to the time evolution of  $We_{slip,x}$  and  $We_{vg}$  for breaking bubbles only, the distribution of these two Weber numbers (shown as black solid symbols in figure 7a,b) for all bubbles are quite close to each other and both peak at around  $We \approx 1$ .

In addition to the Weber numbers, figure 8 shows the alignment of the slip velocity with the semi-major axis of the bubble for (i) all bubbles, (ii) the breaking bubbles ( $5\tau_{\eta}$  prior to the breakup) and (iii) the breaking bubbles ( $20\tau_{\eta}$  prior to the breakup). The results suggest a consistent trend of the bubble semi-major axis flipping from a perpendicular to a parallel orientation relative to the slip velocity direction, which seems to contradict the discussion in § 3.1 that slip velocity should flatten rather than elongate the bubble along its direction.

This surprising behaviour will be explained later after discussing the relative orientation of the bubble semi-major axis with the eigenvectors of the strain rate tensor. Figure 9(a) shows the distribution of the alignment of the bubble semi-major axis with  $\hat{e}_3$  similar to figure 5(b). Here, the distribution is shown as a function of the time before the breakup event. As we discussed in § 3.1, the bubble semi-major axis prefers a slightly perpendicular orientation with  $\hat{e}_3$ . Unlike with slip velocity, this preference becomes even stronger as bubbles approach breakup over time, which is clear from figure 9(a).

Although the distribution of  $We_{vg}$  measuring the magnitude of the driving force changes by little over time (figure 7), the strain rate seems to more effectively compress the bubble as  $\hat{e}_3$  becomes more perpendicular to  $\hat{r}_1$  and better aligns with  $\hat{r}_3$  over time; however, the p.d.f.s of the relative orientation are noisy due to the limited number of breakup events. To verify this observed trend, figure 9(b) shows the p.d.f. for the same relative orientation but only for cases when bubbles experienced significant deformation ( $\alpha > 2.5$ ) but did not break, and the results show a similar trend to what has been observed for breaking bubbles close to the breakup moment. This supports the conjecture that the flow compression

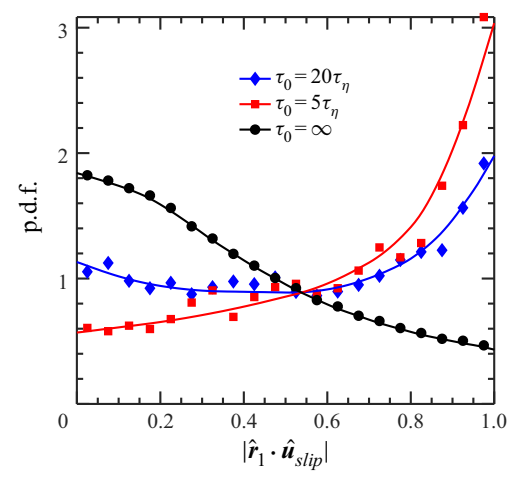


Figure 8. Probability density function of the cosine of the angle between the bubble semi-major axis  $\hat{r}_1$  and the slip velocity  $\hat{u}_{slip}$  for mild deformation and two different time ( $\tau_0$ ) before breakup.

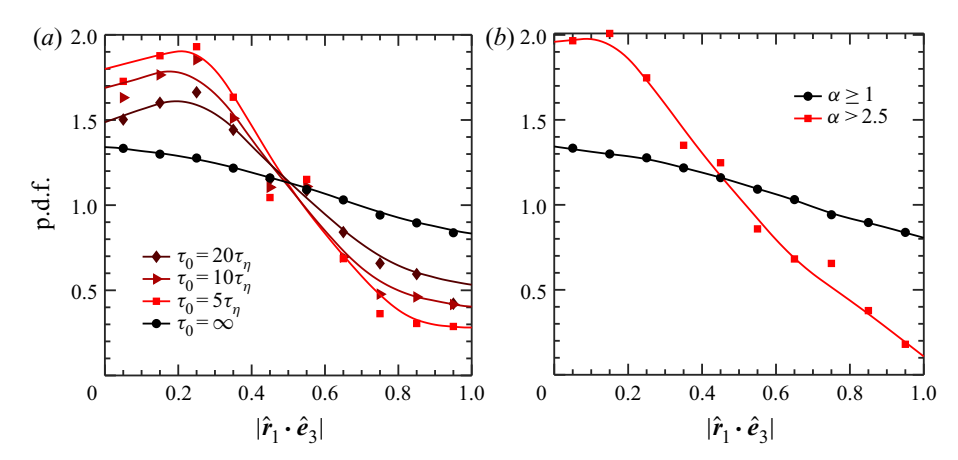


Figure 9. Probability density function of the cosine of the angle between the bubble semi-major axis  $\hat{r}_1$  and the smallest eigenvector of the strain-rate tensor  $\hat{e}_3$  for (a) different times ( $\tau_0$ ) before breakup and (b) all strongly deformed (aspect ratio  $\alpha > 2.5$ ) cases.

around bubbles does not become larger, but becomes more effective as it better aligns with bubbles as they approach breakup or strong deformation.

Based on the observation of the relative orientation between  $\hat{r}_1$  and the slip velocity ( $\hat{u}_{slip}$ ) or between  $\hat{r}_1$  and the strain rate ( $\hat{e}_3$ ), before bubbles break, the slip velocity becomes stronger in magnitude, and the velocity gradient aligns better with bubbles and consequently breaks the bubble more effectively. Each mechanism seems to adjust in a different manner to aid breakup. The surprising nearly 90° rotation of the relative orientation between the slip velocity and  $\hat{r}_1$  is caused by the fact that the slip velocity contains contributions from both bubbles and their surrounding flows. When the bubble deformation is weak, the slip velocity serves as the driving mechanism for bubble deformation. As bubbles approach breakup and deform significantly, their velocity increases and overtakes the direction of the slip velocity. Because the bubble velocity during strong deformation aligns with  $\hat{r}_1$ , the slip velocity

becomes aligned with the semi-major axis. In other words, the slip velocity transitions from the driving mechanism to the driven result owing to the contributions from both phases.

The measured orientational dynamics during deformation and breakup paints a different physical picture compared with the popular bubble-eddy collision model, which is used extensively in the population balance equation to calculate the bubble breakup probability (Luo & Svendsen 1996; Lehr, Millies & Mewes 2002; Wang, Wang & Jin 2003; Liao & Lucas 2009). This model assumes that bubble breakup is driven by the collision with turbulent eddies of size equal to or smaller than the bubble size, and it has to assume a breakup criteria based on the difference or ratio between the eddy kinetic energy and the surface energy, which is similar to the critical Weber number criteria. In the bubble-eddy collision model, the contribution of the slip velocity was not considered, although it represents an important deformation mechanism for finite-sized bubbles, as shown in our work. The bubble-eddy collision model also implies that the Weber number should increase when the bubble encounters a strong eddy; however, we observed no change in the distribution of the Weber number based on the strain rate as bubbles approach breakup. Instead, the bubble orientation shows better alignment with the local strain rate to facilitate bubble breakup. Furthermore, although the slip velocity plays a more dominant role in determining the orientation of weakly deformed bubbles, the strain rate tensor seems to be more important for breaking bubbles. It remains unclear why these two mechanisms switch their roles between deformation and breakup, and thus requires further investigation to appropriately capture it in models.

#### 4. Conclusion

This paper describes an experimental study of the orientational dynamics of deformed finite-sized bubbles in homogeneous and isotropic turbulence with a large energy dissipation rate. Both the bubble geometry and many surrounding tracer particles have been simultaneously reconstructed and tracked in three dimensions. From this unique data set, the relative orientation between bubbles and two driving mechanisms, i.e. slip velocity and the strain rate, can be extracted.

For mild deformation, the strongest alignment is observed between the bubble semi-minor axis and slip velocity, which suggests that bubbles are predominately compressed by the slip velocity. In addition, the bubble semi-major and semi-minor axes are aligned with the strongest stretching and compression directions of the strain rate tensor coarse-grained at the bubble size, respectively. Compared to the relative orientation of the bubbles with the slip velocity, their alignment with the strain rate tensor is weaker and could be affected by the competition between deformation driven by the strain rate and deformation driven by the slip velocity.

The orientational dynamics of deformable bubbles are also compared to that of neutrally buoyant sub-Kolmogorov-scale material elements with no surface tension or slip velocity. Their orientations show strong alignment with the vorticity vector and the intermediate eigenvector of the turbulent strain rate. But such an alignment is absent for finite-sized bubbles in our experiments. This observed difference qualitatively agrees with a previous simulation on sub-Kolmogorov-scale droplets with different capillary numbers, indicating that the restoring force from the surface tension could strongly affect the bubble orientation.

Finally, the orientational dynamics of strongly deformed bubbles is studied, particularly for events near breakup. As bubbles approach breakup, the preference for a perpendicular orientation between  $\hat{e}_3$  and  $\hat{r}_1$  grows, which leads to a more effective

strain-induced deformation. The alignment between  $\hat{u}_{slip}$  and the bubble semi-major axis  $(\hat{r}_1)$  transitions from perpendicular to aligned. This transition was explained by the slip velocity switching from a driving mechanism to the driven result as the strong deformation begins to affect the bubble translational velocity.

**Funding.** We acknowledge the financial support from the National Science Foundation under the award numbers 1854475 and CAREER-1905103.

Declaration of interests. The authors report no conflict of interest.

#### Author ORCIDs.

D Rui Ni https://orcid.org/0000-0002-7178-1479.

#### REFERENCES

- ARMANDOOST, P., BAYAREH, M. & NADOOSHAN, A.A. 2018 Study of the motion of a spheroidal drop in a linear shear flow. *J. Mech. Sci. Technol.* **32** (5), 2059–2067.
- ASHURST, W.T, KERSTEIN, A.R., KERR, R.M. & GIBSON, C.H. 1987 Alignment of vorticity and scalar gradient with strain rate in simulated Navier–Stokes turbulence. *Phys. Fluids* **30** (8), 2343–2353.
- BALACHANDAR, S. & EATON, J.K. 2010 Turbulent dispersed multiphase flow. *Annu. Rev. Fluid Mech.* 42, 111–133.
- BELLANI, G. & VARIANO, E.A. 2012 Slip velocity of large neutrally buoyant particles in turbulent flows. *New J. Phys.* 14 (12), 125009.
- BENZI, R., BIFERALE, L., CALZAVARINI, E., LOHSE, D. & TOSCHI, F. 2009 Velocity-gradient statistics along particle trajectories in turbulent flows: the refined similarity hypothesis in the Lagrangian frame. *Phys. Rev.* E **80** (6), 066318.
- BIFERALE, L., MENEVEAU, C. & VERZICCO, R. 2014 Deformation statistics of sub-Kolmogorov-scale ellipsoidal neutrally buoyant drops in isotropic turbulence. *J. Fluid Mech.* **754**, 184–207.
- BRENNEN, C.E. 1982 A review of added mass and fluid inertial forces. Tech. Rep. CR 82.010.
- Brennen, C.E. 2005 Fundamentals of Multiphase Flow. Cambridge University Press.
- CHEVILLARD, L. & MENEVEAU, C. 2013 Orientation dynamics of small, triaxial–ellipsoidal particles in isotropic turbulence. *J. Fluid Mech.* **737**, 571–596.
- CISSE, M., HOMANN, H. & BEC, J. 2013 Slipping motion of large neutrally buoyant particles in turbulence. J. Fluid Mech. 735, R1.
- CLIFT, R., GRACE, J.R. & WEBER, M.E. 2005 Bubbles, Drops, and Particles. Courier Corporation.
- DE SILVA, I.P.D. & FERNANDO, H.J.S. 1994 Oscillating grids as a source of nearly isotropic turbulence. *Phys. Fluids* 6 (7), 2455–2464.
- ELGHOBASHI, S. 2019 Direct numerical simulation of turbulent flows laden with droplets or bubbles. *Annu. Rev. Fluid Mech.* **51**, 217–244.
- ELLINGSEN, K. & RISSO, F. 2001 On the rise of an ellipsoidal bubble in water: oscillatory paths and liquid-induced velocity. *J. Fluid Mech.* **440**, 235–268.
- ERN, P., RISSO, F., FABRE, D. & MAGNAUDET, J. 2012 Wake-induced oscillatory paths of bodies freely rising or falling in fluids. *Annu. Rev. Fluid Mech.* 44, 97–121.
- FEIGL, K., MEGIAS-ALGUACIL, D., FISCHER, P. & WINDHAB, E.J. 2007 Simulation and experiments of droplet deformation and orientation in simple shear flow with surfactants. *Chem. Engng Sci.* **62** (12), 3242–3258.
- GIRIMAJI, S.S. & POPE, S.B. 1990 Material-element deformation in isotropic turbulence. *J. Fluid Mech.* 220, 427–458.
- GUIDO, S. & GRECO, F. 2001 Drop shape under slow steady shear flow and during relaxation. Experimental results and comparison with theory. *Rheol. Acta* **40** (2), 176–184.
- HUANG, M.-J. 1996 Correlations of vorticity and material line elements with strain in decaying turbulence. *Phys. Fluids* **8** (8), 2203–2214.
- HUBER, C., Su, Y., NGUYEN, C.T., PARMIGIANI, A., GONNERMANN, H.M. & DUFEK, J. 2014 A new bubble dynamics model to study bubble growth, deformation, and coalescence. *J. Geophys. Res.* 119 (1), 216–239.
- KAMEDA, M., KATSUMATA, T. & ICHIHARA, M. 2008 Deformation of bubbles in a highly viscous pipe flow. *Fluid Dyn. Res.* **40** (7–8), 576.
- KOLMOGOROV, A.N. 1941 The local structure of turbulence in incompressible viscous fluid for very large reynolds numbers. *C. R. Acad. Sci.* **30**, 301–305.

- LAMB, H. 1924 Hydrodynamics. Cambridge University Press.
- LEGENDRE, D., ZENIT, R. & VELEZ-CORDERO, J.R. 2012 On the deformation of gas bubbles in liquids. *Phys. Fluids* **24** (4), 043303.
- LEHR, F., MILLIES, M. & MEWES, D. 2002 Bubble-size distributions and flow fields in bubble columns. *AIChE J.* **48** (11), 2426–2443.
- LIAO, Y. & LUCAS, D. 2009 A literature review of theoretical models for drop and bubble breakup in turbulent dispersions. *Chem. Engng Sci.* **64** (15), 3389–3406.
- LUEWISUTTHICHAT, W., TSUTSUMI, A. & YOSHIDA, K. 1997 Chaotic hydrodynamics of continuous single-bubble flow systems. *Chem. Engng Sci.* **52** (21–22), 3685–3691.
- LUNDE, K. & PERKINS, R.J. 1998 Shape oscillations of rising bubbles. In *In Fascination of Fluid Dynamics*, pp. 387–408. Springer.
- Luo, H. & Svendsen, H.F. 1996 Theoretical model for drop and bubble breakup in turbulent dispersions. *AIChE J.* **42** (5), 1225–1233.
- MAFFETTONE, P.L. & MINALE, M. 1998 Equation of change for ellipsoidal drops in viscous flow. J. Non-Newtonian Fluid Mech. 78 (2–3), 227–241.
- MAGNAUDET, J. & EAMES, I. 2000 The motion of high-Reynolds-number bubbles in inhomogeneous flows. *Annu. Rev. Fluid Mech.* **32** (1), 659–708.
- MASUK, A.U.M., SALIBINDLA, A.K.R. & NI, R. 2021 Simultaneous measurements of deforming Hinze-scale bubbles with surrounding turbulence. *J. Fluid Mech.* **910**, A21.
- MASUK, A.U.M., SALIBINDLA, A. & NI, R. 2019a A robust virtual-camera 3D shape reconstruction of deforming bubbles/droplets with additional physical constraints. *Intl J. Multiphase Flow* **120**, 103088.
- MASUK, A.U.M., SALIBINDLA, A., TAN, S. & NI, R. 2019b V-ONSET (Vertical Octagonal Noncorrosive Stirred Energetic Turbulence): a vertical water tunnel with a large energy dissipation rate to study bubble/droplet deformation and breakup in strong turbulence. *Rev. Sci. Instrum.* 90 (8), 085105.
- MATHAI, V., LOHSE, D. & SUN, C. 2020 Bubble and buoyant particle laden turbulent flows. *Annu. Rev. Condens. Matter Phys.* 11, 529–559.
- MEGÍAS-ALGUACIL, D., FISCHER, P. & WINDHAB, E.J. 2006 Determination of the interfacial tension of low density difference liquid–liquid systems containing surfactants by droplet deformation methods. *Chem. Engng Sci.* 61 (5), 1386–1394.
- MORDANT, N., CRAWFORD, A.M. & BODENSCHATZ, E. 2004 Experimental Lagrangian acceleration probability density function measurement. *Physica* D **193** (1–4), 245–251.
- MOUGIN, G. & MAGNAUDET, J. 2001 Path instability of a rising bubble. Phys. Rev. Lett. 88 (1), 014502.
- MÜLLER-FISCHER, N., TOBLER, P., DRESSLER, M., FISCHER, P. & WINDHAB, E.J. 2008 Single bubble deformation and breakup in simple shear flow. *Exp. Fluids* **45** (5), 917–926.
- NI, R., HUANG, S.-D. & XIA, K.-Q. 2012 Lagrangian acceleration measurements in convective thermal turbulence. *J. Fluid Mech.* **692**, 395–419.
- NI, R., KRAMEL, S., OUELLETTE, N.T. & VOTH, G.A. 2015 Measurements of the coupling between the tumbling of rods and the velocity gradient tensor in turbulence. *J. Fluid Mech.* 766, 202–225.
- NI, R., OUELLETTE, N.T. & VOTH, G.A. 2014 Alignment of vorticity and rods with Lagrangian fluid stretching in turbulence. *J. Fluid Mech.* **743**, R3.
- PARSA, S., CALZAVARINI, E., TOSCHI, F. & VOTH, G.A. 2012 Rotation rate of rods in turbulent fluid flow. *Phys. Rev. Lett.* **109** (13), 134501.
- PUMIR, A., BODENSCHATZ, E. & Xu, H. 2013 Tetrahedron deformation and alignment of perceived vorticity and strain in a turbulent flow. *Phys. Fluids* **25** (3), 035101.
- QI, Y., MASUK, A.U.M. & NI, R. 2020 Towards a model of bubble breakup in turbulence through experimental constraints. *Intl J. Multiphase Flow* **132**, 103397.
- RAVELET, F., COLIN, C. & RISSO, F. 2011 On the dynamics and breakup of a bubble rising in a turbulent flow. *Phys. Fluids* **23** (10), 103301.
- RIBOUX, G., RISSO, F. & LEGENDRE, D. 2010 Experimental characterization of the agitation generated by bubbles rising at high Reynolds number. *J. Fluid Mech.* **643**, 509–539.
- RUST, A.C. & MANGA, M. 2002 Bubble shapes and orientations in low Re simple shear flow. *J. Colloid Interface Sci.* **249** (2), 476–480.
- SALIBINDLA, A.K.R., MASUK, A.U.M., TAN, S. & NI, R. 2020 Lift and drag coefficients of deformable bubbles in intense turbulence determined from bubble rise velocity. *J. Fluid Mech.* **894**, A20.
- SCHANZ, D., GESEMANN, S. & SCHRÖDER, A. 2016 Shake-the-box: Lagrangian particle tracking at high particle image densities. *Exp. Fluids* **57** (5), 70.
- SHIN, M. & KOCH, D.L. 2005 Rotational and translational dispersion of fibres in isotropic turbulent flows. *J. Fluid Mech.* **540**, 143–173.

- SPANDAN, V., LOHSE, D. & VERZICCO, R. 2016 Deformation and orientation statistics of neutrally buoyant sub-Kolmogorov ellipsoidal droplets in turbulent Taylor–Couette flow. *J. Fluid Mech.* **809**, 480–501.
- SPANDAN, V., VERZICCO, R. & LOHSE, D. 2017 Deformable ellipsoidal bubbles in Taylor–Couette flow with enhanced Euler–Lagrangian tracking. *Phys. Rev. Fluids* 2 (10), 104304.
- SRDIC, A., FERNANDO, H.J.S. & MONTENEGRO, L. 1996 Generation of nearly isotropic turbulence using two oscillating grids. *Exp. Fluids* **20** (5), 395–397.
- TAN, S., SALIBINDLA, A., MASUK, A.U.M. & NI, R. 2020 Introducing openLPT: new method of removing ghost particles and high-concentration particle shadow tracking. *Exp. Fluids* **61** (2), 47.
- TAYLER, A.B., HOLLAND, D.J., SEDERMAN, A.J. & GLADDEN, L.F. 2012 Exploring the origins of turbulence in multiphase flow using compressed sensing MRI. *Phys. Rev. Lett.* **108** (26), 264505.
- VARIANO, E.A., BODENSCHATZ, E. & COWEN, E.A. 2004 A random synthetic jet array driven turbulence tank. *Exp. Fluids* **37** (4), 613–615.
- VOTH, G.A. & SOLDATI, A. 2017 Anisotropic particles in turbulence. Annu. Rev. Fluid Mech. 49, 249–276.
- WANG, T., WANG, J. & JIN, Y. 2003 A novel theoretical breakup kernel function for bubbles/droplets in a turbulent flow. *Chem. Engng Sci.* **58** (20), 4629–4637.
- XU, H., PUMIR, A. & BODENSCHATZ, E. 2011 The Pirouette effect in turbulent flows. *Nat. Phys.* 7 (9), 709–712.